# Observation of Topological Hall Effect and Nernst Effect in the Canted Antiferromagnetic Phase of $MnBi_2Te_4$

Haiyang Yang[1,7,†], Junwu Huang[1,†], Shangjie Tian[5], Keqi Xia[1], Zhouliang Wang[1], Yuwei Zhang[1], Jiajun Ma[1], Hanjie Guo[6], Xuefeng Zhang[7], Jianhui Dai[1], Yongkang Luo[2,*], Shouguo Wang[5], Hechang Lei[3,4,*], and Yuke Li[1,*]

[1]*School of Physics and Hangzhou Key Laboratory of Quantum Matters, Hangzhou Normal University, Hangzhou 311121, China*
[2]*Wuhan National High Magnetic Field Center and School of Physics, Huazhong University of Science and Technology, Wuhan 430074, China*
[3]*School of Physics and Beijing Key Laboratory of Optoelectronic Functional Materials and MicroNano Devices, Renmin University of China, Beijing 100872, China*
[4]*Key Laboratory of Quantum State Construction and Manipulation (Ministry of Education), Renmin University of China, Beijing 100872, China*
[5]*Anhui Key Laboratory of Magnetic Functional Materials and Devices, School of Materials Science and Engineering, Anhui University, Hefei 230601, China*
[6]*Songshan Lake Materials Laboratory, Dongguan 523808, China*
[7]*Institute of Advanced Magnetic Materials, College of Materials and Environmental Engineering, Hangzhou Dianzi University, Hangzhou 310012, China*

(Received 24 April 2025; accepted manuscript online 16 June 2025)

In magnetic topological materials, the interplay between magnetism and nontrivial topology gives rise to exotic quantum transport phenomena, including the anomalous Hall effect and anomalous Nernst effect. Here, we report the observation of intrinsic topological Hall and topological Nernst effects below the Néel temperature ($T_N = 25\,K$) in the antiferromagnetic (AFM) topological insulator $MnBi_2Te_4$. The maximum of topological Hall resistivity reaches approximately $9\,\mu\Omega\cdot$cm at 2 K, while the topological Nernst signal attains a peak value of $0.1\,\mu V/K$ near 10 K. These anomalous transport behaviors originate from the net Berry curvature induced by the non-collinear spin structure in the canted AFM state. Our results suggest a close connection between the topological thermoelectric effect and non-collinear AFM order in AFM topological insulators.

DOI: 10.1088/0256-307X/42/8/080706 CSTR: 32039.14.0256-307X.42.8.080706

*1. Introduction.* The recent discovery of novel quantum phenomena in intrinsic magnetic topological materials (MTMs), including the axion insulating state,[1] quantum anomalous Hall effect (AHE),[2] and topological magnetoelectric effect,[3] has sparked tremendous research interest in condensed matter physics. Owing to their intertwined nontrivial band topology and magnetic ordering, MTMs provide an ideal platform for both realizing and investigating exotic quantum states and emergent quasiparticles.[4] A diverse array of MTMs—spanning magnetic topological insulators (e.g., $MnBi_2Te_4$[5–7]), Dirac/Weyl semimetals ($Fe_3Sn_2$,[8,9] $Co_3Sn_2S_2$,[10,11] and $Mn_3Sn$[12,13]), Chern-gap topological magnets ($TbMn_6Sn_6$[14,15]), and kagome antiferromagnetic (AFM) compounds (FeGe[16–18])—have demonstrated intrinsic AHEs accompanied by topological Hall/Nernst effects, all originating from nontrivial Berry curvature distributions.

Theoretical models indicate that the intrinsic AHE is dominated by the integral of Berry curvature over all occupied bands, while the anomalous Nernst effect (ANE) is governed predominantly by the Berry curvature near the Fermi level.[19,20] In momentum space, the Berry curvature associated with topological bands gives rise to intrinsic AHE, scaling proportionally with magnetization. Conversely, in real space, non-collinear or non-coplanar spin textures with finite scalar spin chirality, such as magnetic skyrmions, act as effective magnetic fields, generating an additional Hall component known as the topological Hall effect (THE).[21,22] The THE is widely regarded as a hallmark of topologically nontrivial spin textures, originating from real-space spin topology rather than momentum-space band topology.[23–25]

Recently, $MnBi_2Te_4$, a rare layered van der Waals material exhibiting both AFM order and nontrivial band topology, was experimentally confirmed as the first intrinsic AFM topological insulator.[26,27] It undergoes an A-type AFM transition at $T_N = 25\,K$, with magnetic moments aligned along the $c$-axis. Application of an external

†These authors contributed equally to this work.
*Corresponding authors. Email: mpzslyk@hust.edu.cn; hlei@ruc.edu.cn; yklee@hznu.edu.cn
© 2025 Chinese Physical Society and IOP Publishing Ltd. All rights, including for text and data mining, AI training, and similar technologies, are reserved.

magnetic field below $T_N$ induces a spin-flop transition followed by a canted antiferromagnetic (CAFM) phase at intermediate fields. Previous study on thin films suggest that this CAFM state hosts field-induced non-collinear spin textures, potentially giving rise to AHE or THE.[28] At higher magnetic fields, type-II Weyl fermions have also been identified in the ferromagnetic (FM) phase of $MnBi_2Te_4$.[28] Consequently, $MnBi_2Te_4$ has emerged as a promising platform for exploring novel topological phases, including quantum AHE, axion insulating states, magnetoelectric effects, and Weyl semimetal states.[29] The coexistence of non-collinear magnetism and Weyl fermions suggests intriguing and unexpected physical phenomena.

In this Letter, we comprehensively investigate magnetization, electrical, and thermal transport properties of $MnBi_2Te_4$. Through systematic Hall and Nernst measurements, we identify intrinsic topological Hall and topological Nernst effects (TNEs) below 25 K in the CAFM state. Above the spin-polarization threshold, the AHE becomes predominant. Remarkably, the topological Hall resistivity reaches approximately 9 μΩ·cm, significantly larger than many known topological magnets. Simultaneously, the topological Nernst signal exhibits a clear maximum near 10 K, demonstrating distinct temperature dependence compared to the THE. Our findings indicate that non-collinear spin structures in $MnBi_2Te_4$ may give rise to real-space Berry curvature effects, thus motivating further exploration of spin-chirality-driven topological transport in magnetic quantum materials.

*2. Experimental Methods.* High-quality single crystals of $MnBi_2Te_4$ were grown using a self-flux method described previously.[30] X-ray diffraction patterns and crystallographic orientations of the single crystals were characterized at room temperature using a Rigaku D/Max-rA diffractometer with Cu $K_\alpha$ radiation. Samples were cut into bar-shaped geometries for measurements. Magnetization data were collected using a superconducting quantum interference device (SQUID) magnetometer. Magnetoresistivity and Hall measurements were performed via the standard four-terminal configuration in a Quantum Design Physical Property Measurement System (PPMS-9). Thermoelectric effects, including longitudinal thermopower and transverse Nernst effect, were measured by a one-heater-two-thermometers technique in the PPMS under high-vacuum conditions ($< 10^{-5}$ Torr). A schematic diagram of the thermoelectric transport measurement setup is shown in Fig. 1(b). Longitudinal resistivity and thermopower are denoted by subscript $xx$, while transverse Hall and Nernst effects use subscript $yx$. To eliminate spurious contributions from voltage contact misalignment, Hall and Nernst data were symmetrized by reversing the magnetic field direction, utilizing the intrinsic field-odd symmetry of the Nernst signal in contrast to the field-even nature of thermopower.

*3. Results and Discussion.* $MnBi_2Te_4$ crystallizes in a rhombohedral structure with space group $R\bar{3}m$ [Fig. 1(a)]. Along the $c$-axis, it consists of stacked Te-Bi-Mn-Te-Bi septuple layers held together by van der Waals interactions.

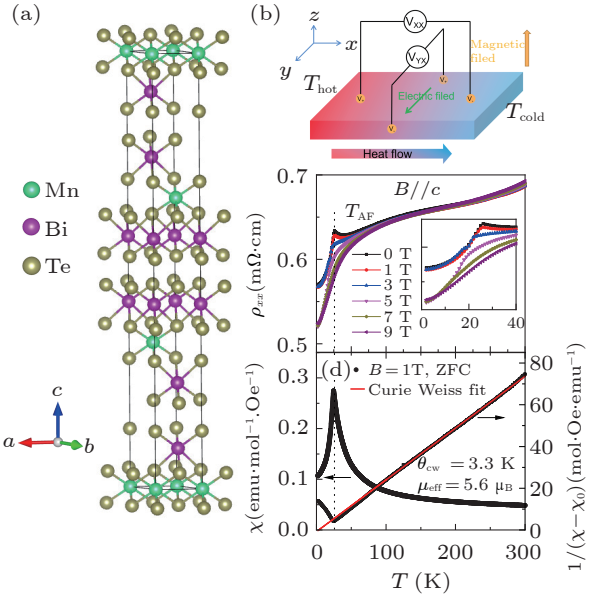


**Fig. 1.** (a) The crystal structure of $MnBi_2Te_4$. (b) A schematic diagram of the thermal-electrical measurements (Seebeck and Nernst effects). (c) Temperature dependence of longitudinal electric resistivity, $\rho_{xx}$, at several magnetic fields. The inset shows an expanded view of the $\rho_{xx}$–$T$ curves in the low-temperature range. (d) (Left) Temperature dependence of magnetic susceptibility $\chi$ with the zero-field-cooling mode at $B = 1$ T. (Right) The black line describes the inverse $(\chi - \chi_0)$ as a function of temperature, and the red line represents the result of the modified Curie–Weiss fit.

The temperature dependence of the longitudinal resistivity $\rho_{xx}$ at zero magnetic field, shown in Fig. 1(c), exhibits metallic behavior throughout the entire measured temperature range, with an evident kink around the Néel temperature ($T_N = 25$ K), consistent with previous reports.[30] This resistivity anomaly near $T_N$ has been attributed to spin scattering.[31] Upon applying a magnetic field parallel to the $c$-axis, the transition peak near $T_N$ is progressively suppressed and shifts toward lower temperatures, eventually broadening into a smooth feature above 5 T. The temperature-dependent magnetic susceptibility $\chi(T)$ under a magnetic field of 1 T measured in the zero-field-cooling mode [Fig. 1(d)] clearly reveals an AFM transition peak at $T_N$, consistent with earlier studies.[31] We fit the high-temperature susceptibility data (100–300 K) using the modified Curie–Weiss law, $\chi(T) = \chi_0 + C/(T - \theta_{CW})$, yielding an effective magnetic moment $\mu_{eff} = 5.6\,\mu_B$/Mn and a Weiss temperature $\theta_{CW} = 3.3$ K. These values closely match previously reported results ($\mu_{eff} \approx 5.0$–$5.9\,\mu_B$/Mn, $\theta_{CW} \approx 1$–6 K).[32,33]

Figures 2(a) and 2(b) display the longitudinal resistivity $\rho_{xx}$ and transverse Hall resistivity $\rho_{yx}$ as functions of the magnetic field $B$ applied along the $c$-axis ($B \parallel c \perp I$) at selected temperatures. Below the Néel temperature ($T_N = 25$ K), $\rho_{xx}(B)$ exhibits two distinct features: (1) A sharp drop at the lower critical magnetic field ($B_1 \approx 3$ T), corresponding to the transition from an A-type AFM state to a CAFM phase, which gradually weakens with increasing temperature; (2) A pronounced kink near the higher critical field ($B_2 \approx 8$ T at 2 K),

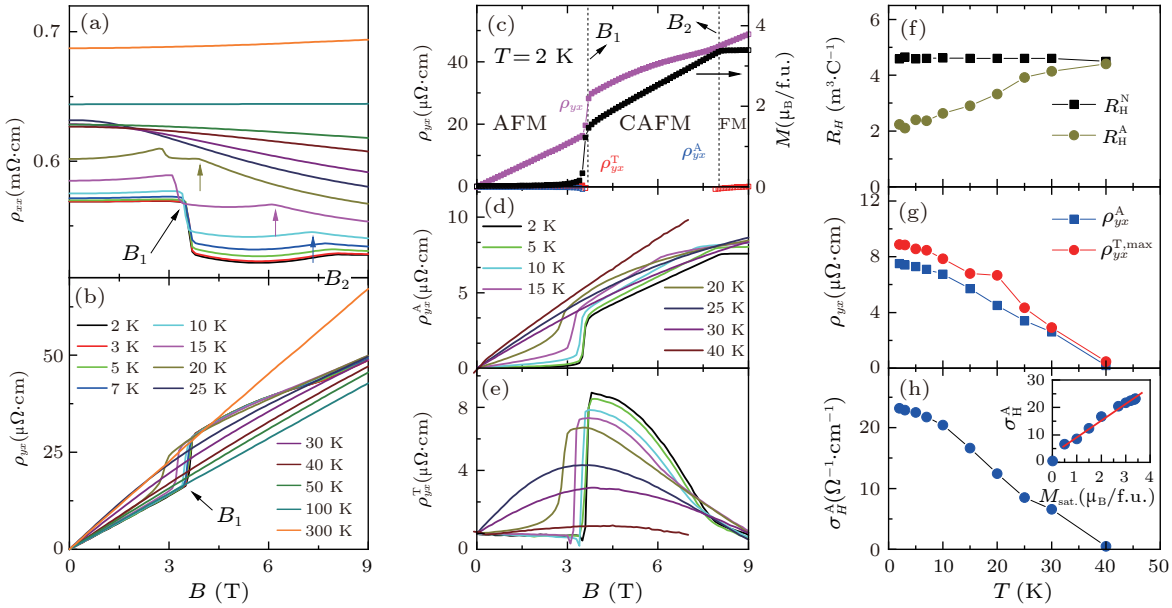


**Fig. 2.** Field dependence of longitudinal resistivity and transverse Hall resistivity at several representative temperatures as $B \parallel c$-axis ($I \perp c$-axis). (a) Logitudinal resistivity $\rho_{xx}$ as a function of magnetic field $B$. (b) Hall resistivity $\rho_{yx}$ vs. magnetic fields. (c) The total Hall resistivity $\rho_{yx}$, AHR $\rho_{yx}^{A}$, and THR $\rho_{yx}^{T}$ as functions of magnetic field at 2 K. (d) Anomalous Hall resistivity $\rho_{yx}^{A}$ and (e) topological Hall resistivity $\rho_{yx}^{T}$ vs. magnetic fields for several selected temperatures below $T_N$. Temperature dependence of (f) Hall coefficient $R_H$, (g) Hall resistivity $\rho_{yx}^{A}$ or $\rho_{yx}^{T,max}$, and (h) Hall conductivity $\sigma_H^A$.

associated with the CAFM-to-FM transition, which broadens and shifts to lower fields as the temperature rises. Below $B_1$, spin fluctuations dominate, whereas above $B_2$, full spin polarization in the FM state suppresses these fluctuations. Consequently, the resistivity sharply decreases with the increasing magnetic field, yielding pronounced negative magnetoresistance at low temperatures. In the intermediate field range ($B_1 < B < B_2$), the system enters a metastable CAFM state, resulting in a steep decrease of $\rho_{xx}(B)$. Notably, negative magnetoresistance persists even above $T_N$, up to around 100 K, which may be attributed to strong spin fluctuations present in the sample. The transverse Hall resistivity $\rho_{yx}(B)$ shown in Fig. 2(b) exhibits a negative slope, indicative of electron-dominated charge transport. In the AFM state ($B < B_1$), $\rho_{yx}$ displays a strictly linear field dependence, reflecting the single-band character of the material. Remarkably, below $T_N$, $\rho_{yx}(B)$ significantly deviates from linearity and exhibits a broad hump between $B_1$ and $B_2$, implying the emergence of a THE in the CAFM phase. This hump progressively weakens with increasing temperature and vanishes above $T_N$, where $\rho_{yx}(B)$ reverts to a linear dependence on magnetic field.

Compared with the magnetization curves $M(B)$ in the CAFM state, the broad humps observed in the Hall resistivity $\rho_{yx}(B)$ clearly deviate from a linear dependence on magnetization, suggesting the emergence of a THE. Thus, the total Hall resistivity can be decomposed into three distinct contributions: $\rho_{yx} = \rho_{yx}^{N} + \rho_{yx}^{A} + \rho_{yx}^{T}$, where $\rho_{yx}^{N} = R_0 B$ represents the normal Hall resistivity linear in magnetic field, $\rho_{yx}^{A} = R_s M$ is the anomalous Hall resistivity associated with magnetization $M$, and $\rho_{yx}^{T}$ denotes the topological Hall resistivity. By fitting the experimental Hall resistivity data to this expression, we isolated these three contributions individually. As an example, Fig. 2(c) presents the extracted anomalous Hall $\rho_{yx}^{A}$ and topological Hall $\rho_{yx}^{T}$ contributions at $T = 2$ K. It is clearly observed that a pronounced $\rho_{yx}^{T}$ emerges within the CAFM state and subsequently diminishes toward zero in the fully polarized FM phase. Similar analyses were conducted at various temperatures, with results summarized in Figs. 2(d) and 2(e) for $\rho_{yx}^{A}$ and $\rho_{yx}^{T}$, respectively. At low temperatures, $\rho_{yx}^{A(B)}$ in Fig. 2(d) exhibits an abrupt jump at $B_1$, followed by a nearly linear behavior below $B_2$, eventually saturating at higher magnetic fields. This feature strongly reflects the close correlation between $\rho_{yx}^{A}$ and magnetization $M$. The normal Hall coefficient $R_H^N$ is negative and remains essentially constant below 40 K, whereas the anomalous Hall coefficient $R_H^A$ slightly increases upon cooling. Using a single-band model, the carrier density is estimated as $n_e = 1/(eR_H^N) \simeq 1.38 \times 10^{20}\,\text{cm}^{-3}$, in good agreement with previous studies.[5]

The anomalous Hall resistivity $\rho_H^A$, extracted from the zero-field intercept of the $\rho_{yx}^{A(B)}$ curves in Fig. 2(d), reaches its maximum value of approximately 8 μΩ·cm at 2 K. The corresponding anomalous Hall conductivity $\sigma_H^A$ is calculated to be about $23\,\Omega^{-1}\cdot\text{cm}^{-1}$, which is comparable to that of frustrate magnets $Nd_2Mo_2O_7$ [34] [See Fig. S1(a) in Supplementary Materials (SM)]. This value is also equivalent to approximately $0.24e^2/(hc)$, where $c = 4.09$ nm is the lattice constant, $e$ is the elementary charge, and $h$ is Planck's constant. Consequently, the anomalous Hall conductivity per Mn layer is estimated as $0.12e^2/h$, comparable to the reported value for the kagome magnet

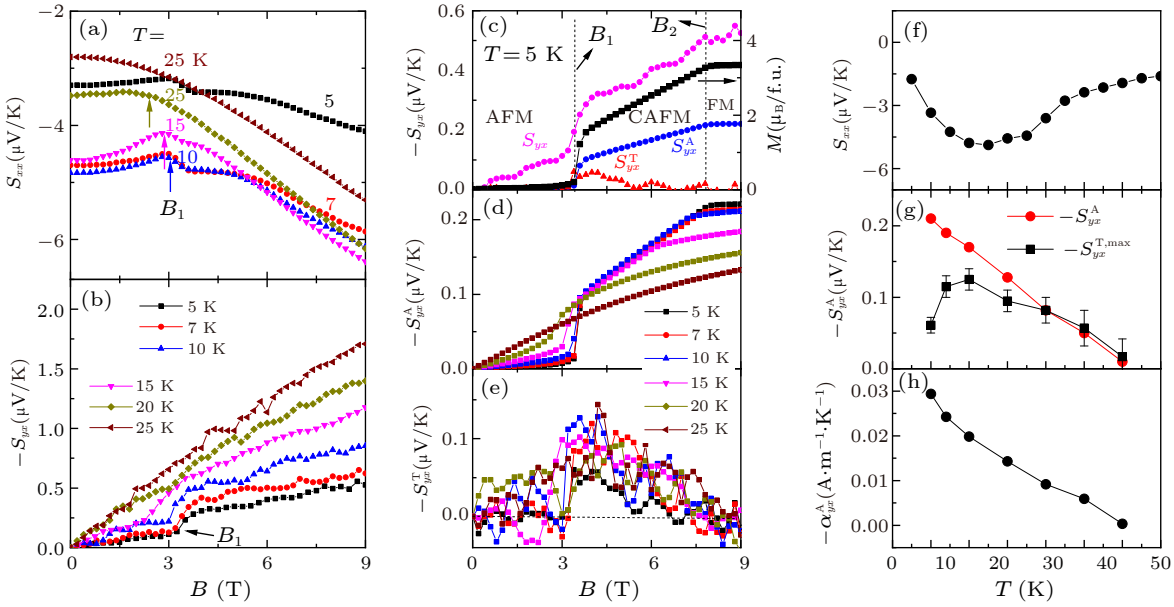


**Fig. 3.** Thermopower and Nernst effect in $MnBi_2Te_4$. (a) Longitudinal thermopower $S_{xx}$ and (b) Nernst signal $-S_{yx}$ as functions of magnetic fields at several representative temperatures. Field dependence of (c) the transverse Nernst signal $-S_{yx}$, (d) $-S_{yx}^{A}$, and (e) $-S_{yx}^{T}$ at several representative temperatures. (f) The $S_{xx}$ as a function of temperature. (g) Temperature dependence of $-S_{yx}^{A}$ and $-S_{yx}^{T,max}$. (h) Temperature dependence of anomalous off-diagonal thermoelectric conductivity $-\alpha_{yx}^{A}$.

$TbMn_6Sn_6$ ($\sim 0.12e^2/h$ per Mn layer), which hosts Chern-gapped Dirac fermions.[14] The inset of Fig. 2(h) further reveals that $\sigma_H^A$ scales linearly with magnetization below $T_N$ and decreases monotonically, approaching zero near 40 K, at which the system transitions into a paramagnetic state.

A prominent topological Hall signal $\rho_{yx}^{T}$ is clearly observed below 40 K [Fig. 2(g)], characterized by a broad hump within the CAFM regime that significantly diminishes as the system approaches the fully polarized FM phase. This feature is attributed to net Berry curvature generated by non-collinear spin textures in the CAFM state, such as the field-induced large THE recently reported in the kagome antiferromagnet FeGe.[18] Similar behavior has also been observed in other systems, including chiral antiferromagnets such as the $Mn_3Ge$ family[35,36] and spin-trimer ferromagnets like $Nd_3Ru_4Al_{12}$.[37] With increasing temperature, the hump in $\rho_{yx}^{T}$ broadens and gradually shifts toward lower magnetic fields. At 2 K, the maximum amplitude of $\rho_{yx}^{T,max}$ reaches about 9 $\mu\Omega\cdot$cm, comparable to previous results reported for $MnBi_2Te_4$[5] and significantly larger than typical values found in other topological magnets, such as the kagome magnet $Mn_3Sn$ ($\sim 0.6\,\mu\Omega\cdot$cm)[36] and the skyrmion-lattice magnet Mn-PdGa ($\sim 0.075\,\mu\Omega\cdot$cm).[38] Notably, a residual topological Hall resistivity persists slightly above $T_N$. This behavior can be attributed to short-range magnetic correlations and fluctuating non-collinear spin arrangements, as observed in AFM $Pt/Cr_2O_3$ bilayers.[39]

We further performed thermoelectric measurements to investigate the exotic topological quantum states in $MnBi_2Te_4$. Specifically, the ANE provides complementary insights into the AHE by directly probing the Berry curvature distribution in momentum space. Figures 3(a) and 3(b) show the longitudinal thermopower $S_{xx}$ and transverse Nernst signal $-S_{yx}$ as functions of magnetic field at selected temperatures. At $T = 5$ K, $|S_{xx}|$ initially decreases with increasing magnetic field up to $B_1$, then exhibits a step-like increase around $B_1$. Beyond this field, $|S_{xx}|$ increases monotonically up to $B = 9$ T, consistent with previous reports.[40] More significantly, the transverse Nernst signal $-S_{yx}(B)$, presented in Fig. 3(c), initially displays a nearly linear field dependence in the AFM phase, followed by a pronounced hump at around $B_1$ within the CAFM region. Subsequently, it reverts to an approximately linear behavior at higher magnetic fields. This behavior strongly resembles the field dependence of the Hall resistivity $\rho_{yx}(B)$ reported previously.[40] With increasing temperature, the hump observed in $-S_{yx}(B)$ broadens and shifts towards lower fields. Above $T_N$, the Nernst signals exhibit an almost linear field dependence. The anomalies observed in both $S_{xx}(B)$ and $-S_{yx}(B)$ at $B_1$ can be attributed to a magnetic structural transition, whereas the broad hump in the CAFM state indicates a field-induced change in electronic structure, resulting in enhanced thermoelectric responses. Specifically, the pronounced anomalous Nernst signal in the CAFM phase provides evidence for the presence of TNE, arising from nonzero Berry curvature induced by non-collinear spin textures with finite scalar spin chirality. Such a scenario has been previously invoked to explain the intrinsic AHE in $MnBi_2Te_4$.[5]

Having confirmed the presence of the THE in the CAFM phase by decomposing the total Hall resistivity, we employ a similar approach to examine its thermoelectric counterpart. In the CAFM state of $MnBi_2Te_4$, the total Nernst signal comprises three contributions: $S_{yx} = S_{yx}^{N} + S_{yx}^{A} + S_{yx}^{T}$, where $S_{yx}^{N} = S_0 B$ is the ordinary Nernst

effect, $S_{yx}^{\mathrm{A}} = S_{\mathrm{s}}M$ denotes the magnetization-dependent ANE, and $S_{yx}^{\mathrm{T}}$ represents the TNE. Analogous to our Hall analysis, we separate the anomalous ($S_{yx}^{\mathrm{A}}$) and topological ($S_{yx}^{\mathrm{T}}$) contributions from the total Nernst signal through data fitting, as illustrated in Fig. 3(c). The extracted anomalous Nernst signal $S_{yx}^{\mathrm{A}}$ at $T = 5\,\mathrm{K}$ shows a prominent magnetic field dependence, characterized by an abrupt jump at $B_1$ followed by saturation above the polarization field $B_2$. This behavior closely parallels the field-dependent magnetization curves. Typically, in conventional ferromagnets, the ANE scales linearly with magnetization $M$, following the relation $|S_{yx}^{\mathrm{A}}| = |Q_{\mathrm{s}}|\mu_0 M$, where $|Q_{\mathrm{s}}|$ is the anomalous Nernst coefficient. Our data suggest that $S_{yx}^{\mathrm{A}}$ in $MnBi_2Te_4$ similarly obeys this scaling relation. With increasing temperature, the jump in $S_{yx}^{\mathrm{A}}(B)$ gradually broadens, and the saturation field $B_2$ decreases monotonically, shrinking the magnetic-field region of the CAFM state [Fig. 3(d)]. Eventually, these features vanish as the system transitions into the paramagnetic phase around 25 K. Interestingly, the topological Nernst signal $S_{yx}^{\mathrm{T}}$, associated with nontrivial Berry curvature, also distinctly emerges as a broad hump within the CAFM phase, but is absent in the fully polarized FM state that hosts Type-II Weyl nodes.[41] Although the magnitude of $S_{yx}^{\mathrm{T}}$ ($\sim$0.1 μV/K) is relatively modest, it remains comparable to that previously reported in $Mn_3Sn$[13] and remains observable up to 25 K.

Figures 3(f)–3(h) present the temperature dependence of the Nernst coefficient and thermopower below 30 K. A slight drop observed at around 25 K in thermopower $S_{xx}$ coincides with the AFM transition, consistent with resistivity measurements. The zero-field anomalous Nernst signal, $-S_{yx}^{\mathrm{A}}$, extracted from Fig. 3(d), increases approximately linearly upon cooling, whereas the maximum topological Nernst signal, $-S_{yx}^{\mathrm{T,max}}$, exhibits a broad peak around 10 K, as shown in Fig. 3(g). Using the thermoelectric relation $-\alpha_{yx}^{\mathrm{A}} = \sigma_H^{\mathrm{A}} S_{xx} + S_{xy}^{\mathrm{A}}\sigma_{xx}$, we obtained the anomalous transverse thermoelectric conductivity $-\alpha_{yx}^{\mathrm{A}}$ displayed in Fig. 3(h). Its magnitude ranges from approximately 0.01 to 0.03 $\mathrm{A{\cdot}m^{-1}{\cdot}K^{-2}}$, comparable to values observed in the two-dimensional van der Waals magnetic topological semimetal $Fe_{3-\delta}GeTe_2$[42] and other classical magnetic topological materials [see Fig. S1(b) in the SM].

Indeed, previous studies have documented the presence of the THE in various spin-textured materials, including skyrmion-lattice systems such as MnSi[43] and FeGe,[18,44] kagome-lattice magnets $YMn_6Sn_6$,[45] $Mn_3Sn$,[46] and $Fe_3Sn_2$,[47,48] as well as frustrated magnets like $Pr_2Ir_2O_7$[49,50] and $Gd_2PdSi_2$.[51] Particularly noteworthy are systems with non-coplanar or non-collinear AFM order exhibiting negligible net magnetization, such as $Mn_5Si_3$[52] and $CoNb_3S_6$.[53] In such AFM systems, non-coplanar spin configurations naturally yield finite scalar spin chirality, defined as $\chi_{ijk} = S_i \cdot (S_j \times S_k)$, generating significant real-space Berry curvature and consequently a pronounced THE. Meanwhile, in momentum space, spin–orbit coupling combined with symmetry breaking lifts spin degeneracy, producing considerable Berry curvature and thus leading to an intrinsic AHE proportional to magnetization.

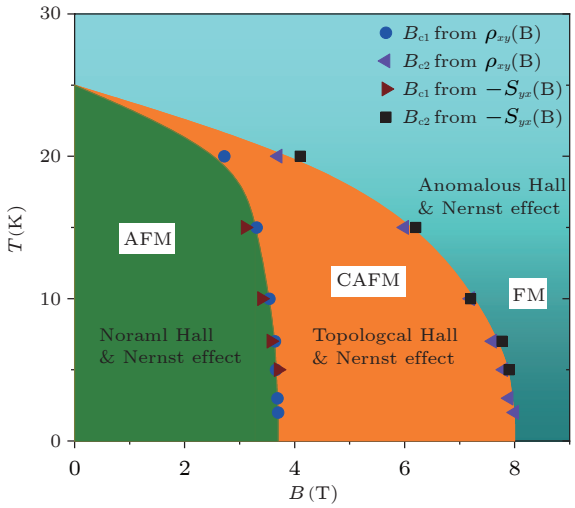


**Fig. 4.** Magnetic-temperature phase diagram of $MnBi_2Te_4$. The colored regions serve as guides to the eye, depicting three distinct magnetic phases: AFM, CAFM, and FM. These phases correspond to regions characterized respectively by the normal Hall and Nernst effects, topological Hall and Nernst effects, and anomalous Hall and Nernst effects. The critical magnetic field, $B_{\mathrm{c}}$, is extracted from Figs. 2(d) and 3(d).

In our $MnBi_2Te_4$ samples, the pronounced THE and TNE signals clearly reflect strong coupling between the electronic structure and non-collinear magnetic order within the CAFM state. The magnetic-temperature phase diagram (Fig. 4) distinctly identifies three magnetic phases, AFM, CAFM, and FM, each characterized by unique transverse transport behaviors. Notably, the CAFM region, featuring non-collinear spin arrangements and finite scalar spin chirality, precisely aligns with the observed topological Hall and Nernst effects. The critical magnetic field $B_{\mathrm{c}}$, systematically extracted from our magneto-transport and magneto-thermal measurements, demarcates transitions among these magnetic phases, further highlighting the close interplay between spin texture evolution and electronic transport phenomena.

*4. Conclusion.* In summary, we have demonstrated the emergence of both THE and TNE in the magnetic Weyl semimetal $MnBi_2Te_4$, originating from non-collinear spin textures in the CAFM phase. The observed topological Hall resistivity reaches $\sim$9 μΩ·cm, while the TNE exhibits a distinct peak value of 0.1 μV/K near 10 K and remains observable up to 25 K. By carefully separating normal, anomalous, and topological contributions, we confirm that both THE and TNE are closely related to scalar spin chirality. Our findings establish $MnBi_2Te_4$ as a versatile platform in which magnetism, electronic topology, and thermal transport are strongly intertwined. Moreover, the observed topological transport signals could be further enhanced through doping, strain engineering, or electrostatic gating, offering exciting prospects for future spintronic and thermoelectric applications based on AFM topological materials.

*Acknowledgements.* This work was supported in part by the Natural Science Foundation of China (Grant No. U1932155). Y Li acknowledges the Hangzhou Joint Fund of the Zhejiang Provincial Natural Science Foundation of China (Grant No. LHZSZ24A040001). Y Luo acknowledges the National Key R&D Program of China (Grant No. 2022YFA1602602). S. Tian acknowledges the China Postdoctoral Science Foundation (Grant No. 2023M730011). H. Lei acknowledges the National Key R&D Program of China (Grant Nos. 2022YFA1403800 and 2023YFA1406500) and the National Natural Science Foundation of China (Grant No. 12274459). This work was also supported by the HZNU Scientific Research and Innovation Team Project (No. TD2025013).

## References

[1] Mogi M, Kawamura M, Yoshimi R, Tsukazaki A, Kozuka Y, Shirakawa N, Takahashi K S, Kawasaki M, and Tokura Y 2017 *Nat. Mater.* **16** 516
[2] Chang C Z, Zhang J S, Feng X, Shen J, Zhang Z C, Guo M H, Li K, Ou Y B, Wei P, Wang L L, Ji Z Q, Feng Y, Ji S H, Chen X, Jia J F, Dai X, Fang Z, Zhang S C, He K, Wang Y Y, Lu L, Ma X C, and Xue Q K 2013 *Science* **340** 167
[3] Dziom V, Shuvaev A, Pimenov A, Astakhov G V, Ames C, Bendias K, Böttcher J, Tkachov G, Hankiewicz E M, Brüne C, Buhmann H, and Molenkamp L W 2017 *Nat. Commun.* **8** 15197
[4] Bernevig B A, Felser C, and Beidenkopf H 2022 *Nature* **603** 41
[5] Lee S H, Zhu Y L, Wang Y, Miao L X, Pillsbury T, Yi H, Kempinger S, Hu J, Heikes C A, Quarterman P, Ratcliff W, Borchers J A, Zhang H D, Ke X L, Graf D, Alem N, Chang C Z, Samarth N, and Mao Z Q 2019 *Phys. Rev. Research* **1** 012011
[6] Zhang H, Xu C Q, Lee S H, Mao Z Q, and Ke X 2022 *Phys. Rev. B* **105** 184411
[7] Morishima Y, Yamaguchi N, Sawahata H, and Ishii F 2023 *Appl. Phys. Express* **16** 043003
[8] Wang Q, Sun S S, Zhang X, Pang F, and Lei H C 2016 *Phys. Rev. B* **94** 075135
[9] Zhang H, Xu C Q, and Ke X L 2021 *Phys. Rev. B* **103** L201101
[10] Liu E, Sun Y, Kumar N, Muechler L, Sun A, Jiao L, Yang S Y, Liu D, Liang A, Xu Q, Kroder J, Sü V, Borrmann H, Shekhar C, Wang Z, Xi C, Wang W, Schnelle W, Wirth S, Chen Y, Goennenwein S T B, and Felser C 2018 *Nat. Phys.* **14** 1125
[11] Yang H Y, You W, Wang J L, Huang J W, Xi C Y, Xu X F, Cao C, Tian M L, Xu Z A, Dai J H, and Li Y K 2020 *Phys. Rev. Mater.* **4** 024202
[12] Nakatsuji S, Kiyohara N, and Higo T 2015 *Nature* **527** 212
[13] Ikhlas M, Tomita T, Koretsune T, Suzuki M T, Nishio-Hamane D, Arita R, Otani Y, and Nakatsuji S 2017 *Nat. Phys.* **13** 1085
[14] Yin J X, Ma W L, Cochran T A, Xu X T, Zhang S T S, Tien H J, Shumiya N, Cheng G M, Jiang K, Lian B, Song Z D, Chang G Q, Belopolski I, Multer D, Litskevich M, Cheng Z J, Yang X P, Swidler B, Zhou H B, Lin H, Neupert T, Wang Z Q, Yao N, Chang T R, Jia S, and Hasan M Z 2020 *Nature* **583** 533
[15] Zhang H D, Koo J, Xu C Q, Sretenovic M, Yan B H, and Ke X L 2022 *Nat. Commun.* **13** 1091
[16] Huang S X and Chien C L 2012 *Phys. Rev. Lett.* **108** 267201
[17] Teng X, Chen L, Ye F, Rosenberg E, Liu Z, Yin J X, Jiang Y X, Oh J S, Hasan M Z, Neubauer K J, Gao B, Xie Y, Hashimoto M, Lu D, Jozwiak C, Bostwick A, Rotenberg E, Birgeneau R J, Chu J H, Yi M, and Dai P 2022 *Nature* **609** 490
[18] Ma J J, Shi C F, Cao Y T, Zhang Y W, Li Y Z, Liao J X, Wang J L, Jiao W H, Guo H J, Xu C C, Cao S X, Dai J H, Bao J K, and Li Y K 2025 *Sci. China Phys. Mech. Astron.* **68** 237412
[19] Xiao D, Yao Y G, Fang Z, and Niu Q 2006 *Phys. Rev. Lett.* **97** 026603
[20] Xiao D, Chang M C, and Niu Q 2010 *Rev. Mod. Phys.* **82** 1959
[21] Yasuda K, Wakatsuki R, Morimoto T, Yoshimi R, Tsukazaki A, Takahashi K S, Ezawa M, Kawasaki M, Nagaosa N, and Tokura Y 2016 *Nat. Phys.* **12** 555
[22] Jiang J, Xiao D, Wang F, Shin J H, Andreoli D, Zhang J X, Xiao R, Zhao Y F, Kayyalha M, Zhang L, Wang K, Zang J D, Liu C X, Samarth N, Chan M H W, and Chang C Z 2020 *Nat. Mater.* **19** 732
[23] Matsuno J, Ogawa N, Yasuda K, Kagawa F, Koshibae W, Nagaosa N, Tokura Y, and Kawasaki M 2016 *Sci. Adv.* **2** e1600304
[24] Vistoli L, Wang W B, Sander A, Zhu Q X, Casals B, Cichelero R, Barthélémy A, Fusil S, Herranz G, Valencia S, Abrudan R, Weschke E, Nakazawa K, Kohno H, Santamaria J, Wu W D, Garcia V, and Bibes M 2019 *Nat. Phys.* **15** 67
[25] Shao Q M, Liu Y W, Yu G Q, Kim S K, Che X Y, Tang C, He Q L, Tserkovnyak Y, Shi J, and Wang K L 2019 *Nat. Electron.* **2** 182
[26] Otrokov M M, Klimovskikh I I, Bentmann H, Estyunin D, Zeugner A, Aliev Z S, Gaß, Wolter A U B, Koroleva A V, Shikin A M, Blanco-Rey M, Hoffmann M, Rusinov I P, Vyazovskaya A Y, Eremeev S V, Koroteev Y M, Kuznetsov V M, Freyse F, Sánchez-Barriga J, Amiraslanov I R, Babanly M B, Mamedov N T, Abdullayev N A, Zverev V N, Alfonsov A, Kataev V, Büchner B, Schwier E F, Kumar S, Kimura A, Petaccia L, Santo G D, Vidal R C, Schatz S, Kißner K, Ünzelmann M, Min C H, Moser S, Peixoto T R F, Reinert F, Ernst A, Echenique P M, Isaeva A, and Chulkov E V 2019 *Nature* **576** 416
[27] Gong Y, Guo J W, Li J H, Zhu K J, Liao M H, Liu X Z, Zhang Q H, Gu L, Tang L, Feng X, Zhang D, Li W, Song C L, Wang L L, Yu P, Chen X, Wang Y Y, Yao H, Duan W H, Xu Y, Zhang S C, Ma X C, Xue Q K, and He K 2019 *Chin. Phys. Lett.* **36** 076801
[28] Bac S K, Koller K, Lux F, Wang J, Riney L, Borisiak K, Powers W, Zhukovskyi M, Orlova T, Dobrowolska M, Furdyna J K, Dilley N R, Rokhinson L P, Mokrousov Y, McQueeney R J, Heinonen O, Liu X, and Assaf B A 2022 *npj Quantum Mater.* **7** 46
[29] Li S, Liu T Y, Liu C, Wang Y Y, Lu H Z, and Xie X C 2024 *Natl. Sci. Rev.* **11** nwac296
[30] Li H, Gao S Y, Duan S F, Xu Y F, Zhu K J, Tian S J, Gao J C, Fan W H, Rao Z C, Huang J R, Li J J, Yan D Y, Liu Z T, Liu W L, Huang Y B, Li Y L, Liu Y, Zhang G B, Zhang P, Kondo T, Shin S, Lei H C, Shi Y G, Zhang W T, Weng H M, Qian T, and Ding H 2019 *Phys. Rev. X* **9** 041039
[31] Cui J H, Shi M Z, Wang H H, Yu F H, Wu T, Luo X G, Ying J J, and Chen X H 2019 *Phys. Rev. B* **99** 155125
[32] Li J H, Li Y, Du S Q, Wang Z, Gu B L, Zhang S C, He K, Duan W H, and Xu Y 2019 *Sci. Adv.* **5** eaaw5685
[33] Zeugner A, Nietschke F, Wolter A U B, GaßS, Vidal R C, Peixoto T R F, Pohl D, Damm C, Lubk A, Hentrich R,

Moser S K, Fornari C, Min C H, Schatz S, Kißner K, Unzelmann M, Kaiser M, Scaravaggi F, Rellinghaus B, Nielsch K, Hess C, Buchner B, Reinert F, Bentmann H, Oeckler O, Doert T, Ruck M, and Isaeva A 2019 *Chem. Mater.* **31** 2795

[34] Taguchi Y, Oohara Y, Yoshizawa H, Nagaosa N, Sasaki T, Awaji S, Iwasa Y, Tayama T, Sakakibara T, Iguchi S, Ohgushi K, Ito T, and Tokura Y 2004 *J. Phys.: Condens. Matter* **16** S599

[35] Nayak A K, Fischer J E, Sun Y, Yan B H, Karel J, Komarek A C, Shekhar C, Kumar N, Schnelle W, Kübler J, Felser C, and Parkin S S P 2016 *Sci. Adv.* **2** e1501870

[36] Li X K, Collignon C, Xu L C, Zuo H K, Cavanna A, Gennser U, Mailly D, Fauqué B, Balents L, Zhu Z W, and Behnia K 2019 *Nat. Commun.* **10** 3021

[37] Kolincio K K, Hirschberger M, Masell J, Gao S, Kikkawa A, Taguchi Y, Arima T, Nagaosa N, and Tokura Y 2021 *Proc. Natl. Acad. Sci. USA* **118** e2023588118

[38] Xiao X, Peng L, Zhao X, Zhang Y, Dai Y, Guo J, Tong M, Li J, Li B, Liu W, Cai J, Shen B, and Zhang Z 2019 *Appl. Phys. Lett.* **114** 142404

[39] Cheng Y, Yu S, Zhu M, Hwang J, and Yang, F 2019 *Phys. Rev. Lett.* **123** 237206

[40] Zhang H, Xu C Q, Lee S H, Mao Z Q, and Ke X 2022 *Phys. Rev. B* **105** 184411

[41] Lee S H, Graf D, Min L J, Zhu Y L, Yi H M, Ciocys S, Wang Y X, Choi E S, Basnet R, Fereidouni A, Wegner A, Zhao Y F, Verlinde K, He J Y, Redwing R, Gopalan V, Churchill H O H, Lanzara A, Samarth N, Chang C Z, Hu J, and Mao Z Q 2021 *Phys. Rev. X* **11** 031032

[42] Yang H Y, Wang Q, Huang J W, Wang Z L, Xia K Q, Cao C, Tian M L, Xu Z A, Dai J H, and Li Y K 2022 *Sci. China-Phys. Mech. Astron.* **65** 117411

[43] Neubauer A, P eiderer C, Binz B, Rosch A, Ritz R, Niklowitz P G, and Boni P 2009 *Phys. Rev. Lett.* **102** 186602

[44] Kanazawa N, Kubota M, Tsukazaki A, Kozuka Y, Takahashi K S, Kawasaki M, Ichikawa M, Kagawa F, and Tokura Y 2015 *Phys. Rev. B* **91** 041122

[45] Wang Q, Neubauer K J, Duan C R, Yin Q W, Fujitsu S, Hosono H, Ye F, Zhang R, Chi S X, Krycka K, Lei H C, and Dai P C 2021 *Phys. Rev. B* **103** 014416

[46] Rout P K, Madduri P V P, Manna S K, and Nayak A K 2019 *Phys. Rev. B* **99** 094430

[47] Li H, Ding B, Chen J, Li Z F, Hou Z P, Liu E K, Zhang H W, Xi X K, Wu G H, and Wang W H 2019 *Appl. Phys. Lett.* **114** 192408

[48] Wang Q, Yin Q W, and Lei H C 2020 *Chin. Phys. B* **29** 017101

[49] Ohtsuki T, Tian Z M, Endo A, Halim M, Katsumoto S, Kohama Y, Kindo K, Lippmaa M, and Nakatsuji S 2019 *Proc. Natl. Acad. Sci. USA* **116** 8803

[50] Guo L, Campbell N, Choi Y, Kim J W, Ryan P J, Huyan H X, Li L Z, Nan T X, Kang J H, Sundahl C, Pan X Q, Rzchowski M S, and Eom C B 2020 *Phys. Rev. B* **101** 104405

[51] Khanh N D, Nakajima T, Yu X Z, Gao S, Shibata K, Hirschberger M, Yamasaki Y, Sagayama H, Nakao H, Peng L C, Nakajima K, Takagi R, Arima T H, Tokura Y, and Seki S 2020 *Nat. Nanotechnol.* **15** 444

[52] Sürgers C, Fischer G, Winkel P, and Löhneysen H V 2014 *Nat. Commun.* **5** 3400

[53] Takagi H, Takagi R, Minami S, Nomoto T, Ohishi K, Suzuki M T, Yanagi Y, Hirayama M, Khanh N D, Karube K, Saito H, Hashizume D, Kiyanagi R, Tokura Y, Arita R, Nakajima T, and Seki S 2023 *Nat. Phys.* **19** 961